

Synergistic wear-corrosion analysis and modelling of nanocomposite coatings

Mian Hammad Nazir^a, Zulfiqar Ahmad Khan^{a,*}, Adil Saeed^b, Arpith Siddaiah^c, Pradeep L. Menezes^c

^a NanoCorr, Energy and Modelling (NCEM) Research Group, Department of Design and Engineering, Bournemouth University Talbot Campus, Poole, Dorset, BH12 5BB, UK

^b Global College of Engineering and Technology, P.O.Box 2546, CPO Ruwi 112, Muscat Sultanate, Oman

^c Mechanical Engineering Department, University of Nevada, Reno, NV 89557, USA

ARTICLE INFO

Keywords:

Nanocomposite coatings
Synergistic wear-corrosion
Wear
Corrosion
Modelling

ABSTRACT

This paper presents analysis and modelling of synergistic wear-corrosion performance of Nickel-Graphene (Ni/GPL) nanocomposite coating and compares it with un-coated steel 1020 under reciprocating-sliding contact. A novel synergistic wear-corrosion prediction model incorporating Archard description with nano-mechanics and electrochemistry was developed for Ni/GPL and steel 1020. The model is equally applicable to any kind of nanocomposite coating and bulk material like metals. For various nanocomposite coatings; their respective mechanical parameters should be used as inputs such as Poisson's ratio (ν), Elastic Modulus (E), Hardness (H), Coefficient of Thermal Elastic mismatch (CTE) and intrinsic grain size (Do). The synergistic wear-corrosion effects were significantly prominent in steel compared to Ni/GPL especially under contaminated lubricating oil conditions. This behaviour of Ni/GPL attributes to compact, refined grain structure leading to minimal grain pull-out during wear cycles which was also assured by less severe micro-ploughing in Ni/GPL compared to severe micro-cutting in steel. The predictions and experimental results were in good-agreement. Modelling of synergistic effects of wear-corrosion applied to nano-composite coatings have never been presented prior to this research. The significance of this work in terms of precision based wear-corrosion synergistic analysis, modelling and predictive techniques is evident from various industrial applications. This work will bring impacts for both in-situ and remote sensor based condition monitoring techniques to automotive, locomotive, aerospace, precision manufacturing and wind turbine industries.

1. Introduction

A nanocomposite coating is a state-of-the-art method of producing highly durable and reliable novel materials at room temperature for current advanced technological applications, for example automotive, defence and aerospace [1,2]. A nanocomposite coating compared to other coating types provides excellent functional properties such as wear and corrosion resistance to the coated surface. The introduction of nano particles in metal matrix had found to be super strong in Tribological strength [3,4]. Various nickel matrix nanocomposite coatings comprising diverse range of inert nano particles such as Al_2O_3 , SiC, ZrO_2 , Graphene (GPL), TiO_2 and diamond, etc., have been electrodeposited by using distinct electrolytes having suspended nanoparticles [5–9].

Synergistic wear-corrosion can be defined as “a process, where the

removal of the material results from combined activities of mechanical and electrochemical mechanisms” [10]. Literature survey shows different numerical models for predicting wear mechanisms under the effects of mechanical and electrochemical parameters [11–19]. Initial wear-corrosion models only included the effects of either wear-on-corrosion or corrosion-on-wear but did not address the synergistic wear-corrosion process [11,12,14,15]. In the last two decades, some advanced synergistic wear-corrosion models were developed as shown in Table 1. A synergistic model developed by Garcia et al. [17] showed the relation of corrosion current density with worn area. Garcia's model was further modified by Goldberg [18] for corrosion currents generated as a result of scratching passive surfaces. Another advanced model was developed by Mischler et al. [19] for reciprocating contacts including the influences of material hardness and load on synergism. The

* Corresponding author.

E-mail address: zkhan@bournemouth.ac.uk (Z.A. Khan).

<https://doi.org/10.1016/j.triboint.2018.01.027>

Received 27 November 2017; Received in revised form 30 December 2017; Accepted 11 January 2018

Available online 3 February 2018

0301-679X/© 2018 The Authors. Published by Elsevier Ltd. This is an open access article under the CC BY-NC-ND license (<http://creativecommons.org/licenses/by-nc-nd/4.0/>).

Nomenclature		
$a_{(i)}$	half width of the contact at the i th wear cycle (m)	$h_C(0)$ thickness of coating at the centre of the wear scar (mm)
$h_{(i)}(X)$	wear depth at the x position of the interface (2D contact) at the i th wear cycle (m)	ζ_r radius of curvature of coating-substrate system due to residual stress (mm^{-1})
K_V	Archard wear coefficient related to the wear volume analysis ($\text{mm}^3 (\text{N m})^{-1}$)	D_o grain size of coating at the time of deposition (nm)
L	axial length of the cylinder/plane contact (mm)	V_W volume loss due to wear (mm^3)
P	normal force (N)	V_C volume loss due to corrosion (mm^3)
P_L	normal force per unit of axial length (2D contact) (N/mm)	ΔV_W change in corrosion volume due to wear (mm^3)
V	wear volume (m^3)	ΔV_C change in corrosion volume due to wear (mm^3)
$W_{(i)}$	Archard factor dissipated during the i th wear (N/m)	K_V wear rate (mm^3/Nm)
$W_H(0)$	Hertzian approximation of the Archard factor during the i th wear cycle (N m/m^2)	K_C corrosion rate (mm/year)
$\sum W$	(accumulated) Archard factor (Nm)	K_{Cw-c} synergistic effect of wear-corrosion on corrosion rate (mm/year)
$\sum W(0)$	(accumulated) Archard factor density dissipated at the centre of the interface ($x = 0$, 2D contact) (N m/m^2)	\overleftarrow{J} corrosion current density (A/mm^2)
P_S	surface porosity (%)	j_o equilibrium exchange current density (A/mm^2)
$\sigma_C(0)$	biaxial surface stress of the coating at $x = 0$ (GPa)	S synergistic factor (mm^3)
E_1, E_2, E_3	elastic moduli of coating, ball and substrate (GPa)	
ΔT	change in temperature from fabrication temperature (K)	
		Greek symbols
		δ displacement (m)
		δg sliding amplitude (m)
		ρ density of the nanocomposite coating material (g/mm^3)

Table 1
Some advanced synergistic wear-corrosion models.

Synergistic wear-corrosion models	Developer	Ref.
$\overleftarrow{J} = i \frac{R}{3} V_W \int_0^t j_o(t) dt + i \frac{R}{3} (V - V_W) \int_0^t j_o(t) dt$	Garcia et al.	[17]
$\overleftarrow{J} = \frac{R j_o}{3} V_W e^{\left[\frac{F n_i}{R T} \right]} + \frac{R \rho Z F V_W}{3 V_m}$	Goldberg	[18]
$\overleftarrow{J} = K Li \frac{P}{H} \left(\frac{P}{H} \right)^{\frac{1}{2}} \int_0^t j_o dt$	Mischler et al.	[19]
$\overleftarrow{J} = \frac{F \rho}{K A_s t} (V - (K_V \sum W) - S)$	Khan-Nazir II	Reported here

\overleftarrow{J} = corrosion current density; i = wear cycles; j_o = equilibrium exchange current density; R = radius of ball; b_a = Tafel slope; n_i = scratch over potential; ρ = coating density; F = Faraday's constant; Z = number of transferred electrons; V = wear-corrosion volume loss; V_W = volume loss owing to wear; V_m = coating molar mass; H = hardness; P = normal loading; K_V = wear rate, K = electrochemical equivalent of specimen material, W = Archard factor density, A_s = area of the specimen, S = synergistic factor.

prediction of synergistic wear-corrosion response of steel 1020 from all the models listed in Table 1 under lubricating oil condition contaminated with sea salt (Medium-II [Table 2]) were compared with the experiment as shown in Fig. 1. Our developed model showed more accurate prediction compared with the conventional models.

The existing synergistic wear-corrosion models [11–19] can predict the synergistic wear-corrosion in only bulk materials (metals) and alloys however predicting the synergistic wear-corrosion performance of nanocomposite coatings is still a grey area in wear modelling. Predicting the effects of intrinsic nano-mechanics parameters, such as the eigentresses, porosity, deposited grainsize and thermal mismatch of nanocomposites on their synergistic wear-corrosion has always been a challenge.

To address the above problem, a novel 2-D synergistic wear-corrosion

Table 2
Three types of lubricating oil conditions used during synergistic wear-corrosion experiments.

Oil Medium	Contaminate induced	Oil Contents
Medium-I	–	oil (uncontaminated)
Medium-II	5%(wt%) sea salt	oil Contaminated with sea salt
Medium-III	5%(wt%) sea salt and 10%(wt%) water	oil Contaminated with sea salt and water

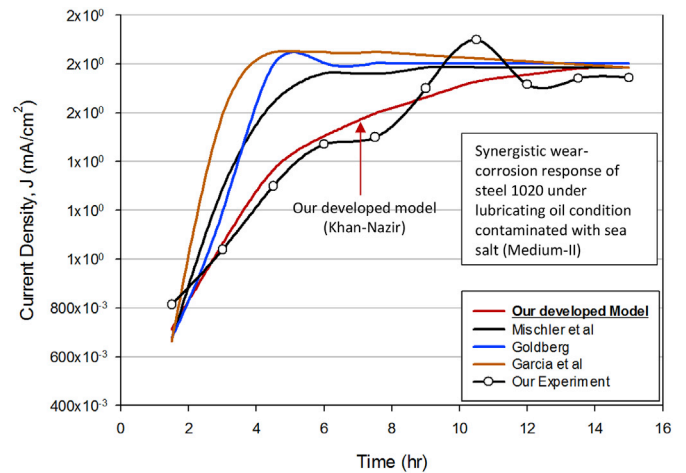


Fig. 1. The comparison of predictions of synergistic wear-corrosion response of steel 1020 from all the models listed in Table 1 under lubricating oil condition contaminated with sea salt.

model for nanocomposite coatings has been formulated by combining the popular Archard equation with the nano-mechanics and the electrochemical equations. The analysis uses gross slip conditions with wear corrosion, focusing on metal interfaces. In this paper the synergistic wear-corrosion performance of nanocomposite coating Ni/GPL was analysed and compared with the performance of un-coated steel 1020. The developed synergistic model can however be equally used for any kind of nanocomposite coating and bulk material. Similar studies in our group on coatings failures have been performed [20–34].

Water and other non-conventional lubrication have been studied in other projects within NCEM, for example [31–34] and is not within the scope of this research. The complexity of rotating electrolyte, inter-electrode spacing and relation to EIS (electro-chemical impedance spectroscopy) with varying constituents as salts, its molality and concentrations by weight percentage are challenging aspects in terms of in-situ corrosion condition monitoring. Previous and existing research projects within NCEM have been investigating marine applications where conventional lubricants are polluted. This includes

non-conventional lubricants such as thermofluids.

It was therefore, necessary to focus on the polluting constituents reference to conventional lubrication and study the synergistic effects. It is also important to note that for greater precision and validation of modelling, incremental variations, in electrochemical process was more preferable than an accelerated simulation when a highly corrosive medium, such as sea water is used. In essence, the focus is; contamination of lubricating oil, incremental EIS data acquisition, optimisation of 3-electrode system and developing a more robust and reliable model.

This research was commenced to examine the following procedures: (1) How the equations for the synergistic wear-corrosion behaviour of nanocomposite coatings be developed by using Archard description combined with nano-mechanics and electrochemical equations? (2) How do the intrinsic nano-mechanics parameters such as the eigenstresses, porosity and grainsize and the electrochemical parameters such as the type and concentration of diffusing corrosive species influence the synergistic wear-corrosion process of the nanocomposite coatings? (3) How can the prediction for synergistic wear-corrosion effect on corrosion rate of nanocomposite coatings be performed, and which intrinsic nano-mechanics parameter influence corrosion rate the most? (4) How to simulate the model and validate its reliability by comparison with the experimental results?

2. Experiment

2.1. Sample preparation

The nanocomposite coating Ni/GPL was deposited over rectangular steel disc samples by using pulse electrodeposition method. The thickness

of coating on the samples was kept $h = 10 \mu\text{m}$. The dimensions and surface roughness of samples was $30 \text{ mm} \times 10 \text{ mm} \times 3 \text{ mm}$ and $0.04 \mu\text{m}$ respectively. Three samples for each test were prepared to ensure repeatability. All samples were surface conditioned by using ultrasonic treatment before coating deposition.

Bath solution containing Nickel(II) Sulfate Hexahydrate, Nickel(II) chloride and Boric acid was used with their individual concentrations of 240 g/L, 57 g/L and 42 g/L respectively. The dispersion of 4–6 nm sized Graphene nanoparticles in a solution was performed by using ultrasonic dispersion devise. The magnetic stirrer was constantly used for 12 h for good particle suspension in a solution prior to the start of coating deposition. The NaOH and diluted H_2SO_4 were used to maintain the pH of solution between 3.0 and 3.5.

The parameters which were set the same throughout the deposition process are: current density = 5 A/dm^2 , on-off pulse time = 30–90 ms and duty cycle = 30%. Pure nickel plate was used as anode and rectangular steel disc was used as cathode. The microstructural characteristics of Ni/GPL have been thoroughly discussed in Ref. [35].

2.2. Testing procedure

Synergistic wear-corrosion experiments were performed by using a modified reciprocating test rig design as shown in Fig. 2. Three conditions of lubricating oil medium were used to perform the synergistic wear-corrosion experiments, listed in Table 2. The purpose for these three conditions was to compare the synergetic wear-corrosion behaviour of Ni/GPL under pure and contaminated oil conditions. Under each condition each experiment was repeated at least three times for repeatability. The experiments were performed for 15 h without interruption.

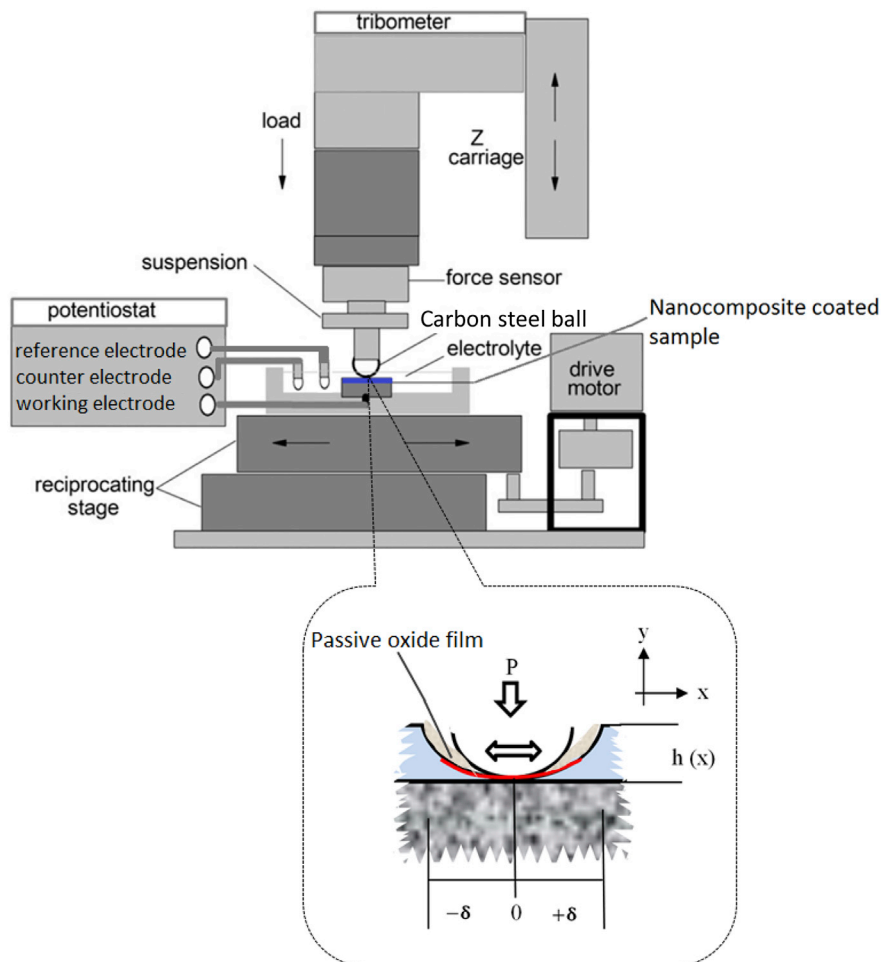


Fig. 2. The schematic of reciprocating test rig setup which was used to perform the synergistic wear-corrosion experiments.

Continuous monitoring of the wear volume and corrosion rates was performed during this duration. For comparative analysis, the synergistic wear-corrosion behaviour of steel 1020 under all three conditions was also examined. The reason of selecting steel 1020 for comparative analysis is its significant applications in bearing industry and its better wear-corrosion performance compared to other grades of steel [36]. The system contact was isolated in three ways during experimentation: the lubricating cup was made up of a non-conductive polymeric material; the experiments were conducted with a thin ceramic plate under the coated sample (working electrode); and the collects used inside the ball holder that isolated the carbon steel ball from the holder were non-metallic.

Reciprocating wear tests were performed against a carbon steel ball ($R = 5$ mm radius) at the normal force P of 15 N with a sliding speed of 0.05 m/sec with a constant 2 Hz frequency and a linear displacement amplitude of $\delta_g = 2$ mm using a test rig (Fig. 2). The test rig was coupled to the test viewer software to monitor the wear-corrosion volume loss. Constant displacement amplitudes δ_g (stroke lengths) were applied, during the tests, characterised by the total number of wear cycles (i). Wear depth at any point along x-axis was denoted as $h(x)$ with respect to the centre at $x = 0$ as shown in bottom Fig. 2. The displacement to the left of $x = 0$ was $-\delta$ while to the right was $+\delta$. Tribo-conditions were chosen to ensure sliding contact subject to the boundary lubrication regime and to permit retrieval of data before coating had completely failed.

ASTM G119-04 standard was followed to determine the synergism between wear and corrosion in each of the three oil conditions. A potentiostat was used to monitor the corrosion rate throughout the synergistic wear-corrosion experiment. The reference electrode (saturated calomel) and the counter electrode were placed near the sample for accurate measurements.

At the end of experiment the samples were kept in oil condition for 2 h to allow the surface re-passivation. After this step the samples were surface conditioned by using ultrasonic treatment before the respective wear tracks were analysed via 3D interferometer, Scanning Electron Microscope (SEM) and Energy Dispersive Spectroscopy EDS.

2.3. Experimental observations

2.3.1. Synergistic wear-corrosion effect

In Table 3, the Post-test EDS micrographs for Ni/GPL and steel 1020 identify the elements and their concentration. EDS for every medium was conducted at least at five spectrum points located inside and outside the wear tracks however for illustration purpose, only one spectrum point is shown at inside and one at outside for each medium. Inside spectrum points were used to compare the wt% loss of elements inside the wear track from outside. The EDS results revealed that for both the Ni/GPL and steel, the highest wt% loss of elements inside the wear tracks was found in Medium-III and the lowest wt% loss was found in Medium-I.

The comparison of EDS results for Ni/GPL and steel showed the higher wt% loss of Fe in steel wear tracks compared to Ni in Ni/GPL wear tracks in all the three mediums. For example, the wt% loss of Fe in Medium-III was 40% compared to 28% loss of Ni. Likewise in Medium-II the wt% loss of Fe was 30% compared 13% loss of Ni. Similarly in Medium-I the wt% loss of Fe was 6% compared 4% loss of Ni. The lower wt% loss of Ni/GPL compared to steel in all the three mediums is linked with its microstructural properties [37]. Ni/GPL has compact, refined grains resulting in minimal transport of corrosive contaminants, water and oxygen which inhibits severe cracking avoiding under coat oxidation, and grain pull-out during wear cycles. Such behaviour of Ni/GPL resulted in small wt% loss compared to steel during synergistic wear-corrosion testing.

Another interesting EDS result is the presence of higher wt% of carbon inside the Ni/GPL wear tracks compared to steel, especially in Medium-II and III. The reason is that in the case of Ni/GPL wear tracks, some of the carbon is coming from the breakdown of carbon chains of graphene in addition to the significant portion of carbon coming from the wear of counter carbon steel ball. The counter carbon steel ball surface

sliding against Ni/GPL exhibited higher wear weight loss (Fig. 3 (a)) compared to steel 1020 (Fig. 3 (b)). This seems to be an indication of somewhat compatible hardness of Ni/GPL (480 HV) [38] as that of counter carbon steel ball hardness (520 HV) [39] compared to steel 1020 hardness (126HV) [40]. The main reason for choosing the carbon steel ball is, its very high hardness (520 HV) and wider industrial applications. High hardness of steel ball is also significant in terms of benchmarking against Ni/Graphene for comparative studies.

The trends for synergistic wear-corrosion effect on corrosion rate (K_{Cw-c}) of both Ni/GPL and steel 1020, as shown in Fig. 4 (a) can be observed to constantly rise in corrosion rates right from the start of experiment in all mediums. Compared to Ni/GPL, steel showed 18.5%, 21.5% and 67.8% higher corrosion rates in Medium-I, II and III respectively. Likewise, in Fig. 4 (b) the synergistic wear-corrosion effect on

current densities J of both Ni/GPL and steel 1020 showed that the current densities (J) stabilised after some time in all the mediums. However, similar to corrosion rates, the current densities were significantly low for Ni/GPL compared to steel. This behaviour of reduction in current densities and corrosion rates of Ni/GPL is attributed to the compact and refine grain structure of Ni/GPL, which prevents oxidation (wear-corrosion) of the Ni/GPL surfaces when present at sliding contact interfaces [41].

Further in case of steel, there were also observed periods of acceleration in corrosion rates (Fig. 4 (a)) and current densities (Fig. 4 (b)) both in Medium-II and Medium-III compared to Medium-I, which are indicative of the steel wear debris inside the wear track. However, in case of Ni/GPL, no such accelerated periods were observed in any of the Mediums which clearly indicate that Ni/GPL remained fairly intact during testing. The significant amount of steel wear debris in Medium-II would have increased the cell medium resistance accelerating the anodic reactions. While in Medium-III, significant amount of clear corrosive compounds including iron oxide were observed because the steel wear debris rapidly reacted with the salt plus water contaminants (forming aqueous NaCl) within the oil. These corrosive compounds interfered with the sliding ball resulting in severe cavitation and starved lubrication regions (Table 4).

The influences of lubricating oil contamination on the width of wear tracks was also analysed by using SEM, as illustrated in Table 4. It can be clearly seen that Ni/GPL exhibited 0.304 mm, 0.518 mm and 0.809 mm wide wear tracks in Medium I, II and III respectively which were significantly small compared to 0.774 mm, 1.11 mm and 2.6 mm steel wear tracks. Moreover, Ni/GPL did not show any visible anomalies along the wear tracks for Medium-II and III, whereas the steel wear tracks exhibited significant cavitation because of contaminants at the sliding ball interface which accelerated the synergistic wear-corrosion effects during testing.

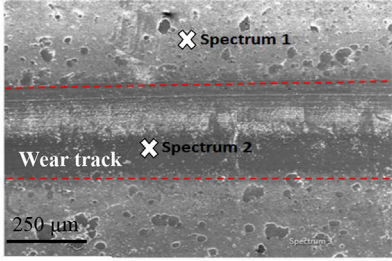
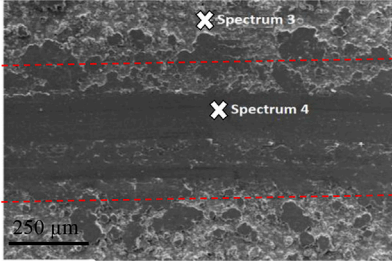
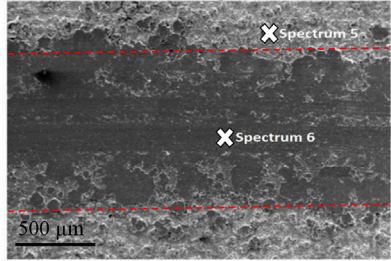
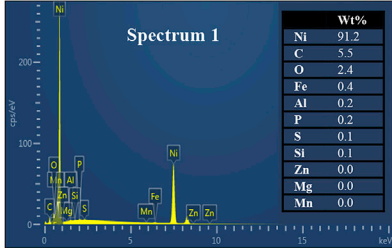
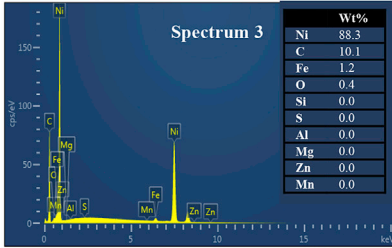
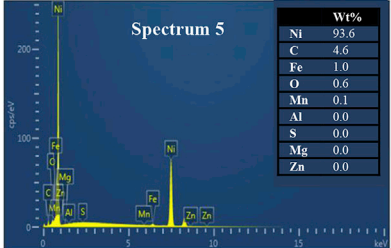
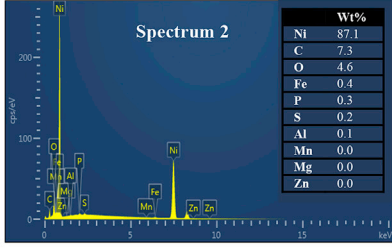
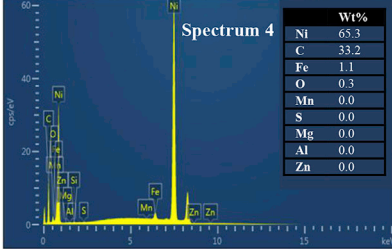
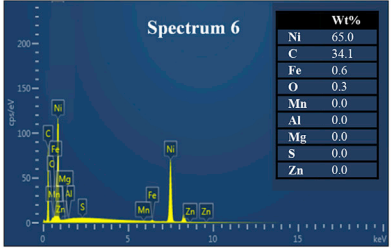
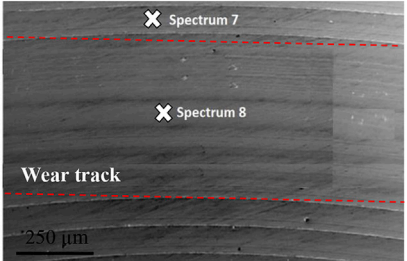
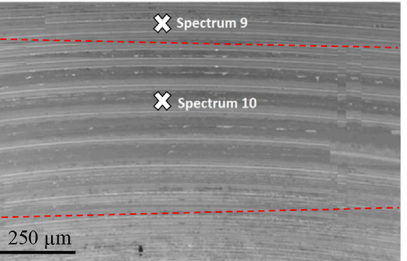
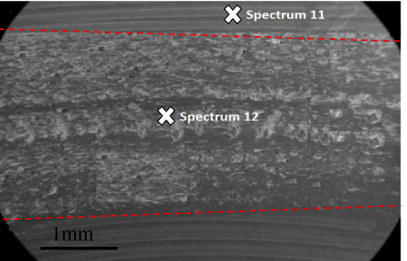
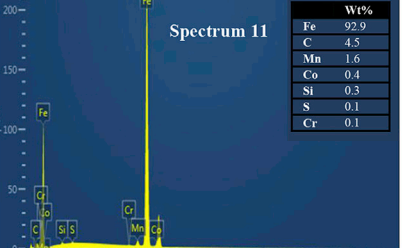
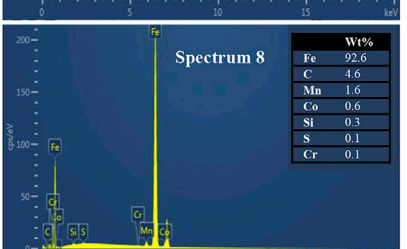
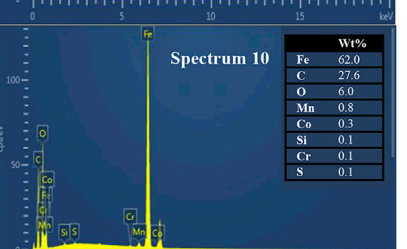
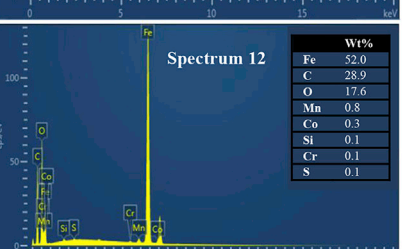
2.3.2. Evolution of corrosion rate without wear

The evolution of corrosion rates (K_C) of both Ni/GPL and steel 1020 without wear showed fairly linear behaviour throughout for all the mediums, as can be observed in Fig. 5. For Ni/GPL, the corrosion rates for all the mediums almost overlapped, showing that Ni/GPL was minimally affected by contaminants. This behaviour of Ni/GPL can be attributed to its compact, refined grain which inhibits the transport of corrosive contaminants, in turn preventing intergranular corrosion. However, the corrosion rates of steel for all the mediums, especially medium-II and III were significantly high. It is worth noting that the corrosion rates of steel without wear did not show accelerated periods of corrosion rates as were seen previously in the case of synergistic wear-corrosion K_{Cw-c} experiment (Fig. 4 (a)). This clearly indicates that the steel 'wear debris' during synergism were responsible for accelerated corrosion rates.

2.3.3. Evolution of wear rate without corrosion

39. The wear rates (K_V) without corrosion for both Ni/GPL and steel 1020 were observed only in Medium-I as it was an uncontaminated

Table 3
The Post-test EDS micrographs for Ni/GPL and steel 1020 identifying the type of elements and their concentration.

Material	Medium-I	Medium-II	Medium-III	
Ni/GPL				
				
				
	Steel 1020			
				
				

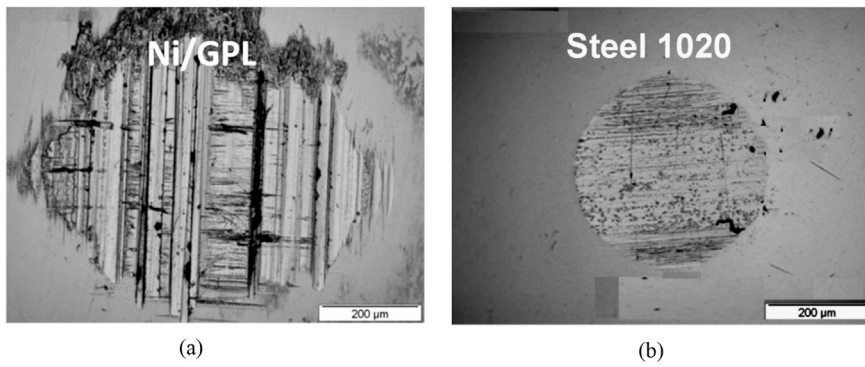


Fig. 3. Microscopic images of counter carbon steel ball surface sliding against Ni/GPL and steel 1020.

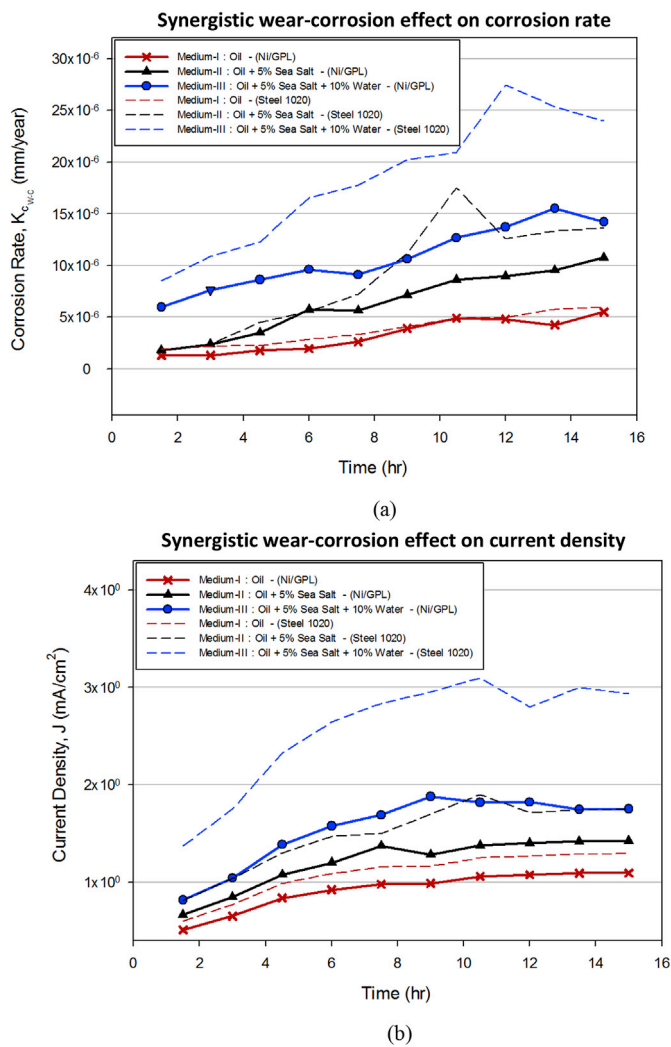


Fig. 4. The synergistic wear-corrosion effect of both Ni/GPL and steel 1020 on (a) corrosion rates $K_{C_{w-c}}$ and (b) current densities J .

medium. Fig. 6 shows the increasing trends of wear rates of Ni/GPL and steel with increasing time and Archard loading factor W . Where, Archard factor (also known as the total dissipated energy during wear cycles) is defined as the multiplication of normal force (P) with total sliding displacement (δ) i.e. $P(N) \times \delta(m)$. Therefore, the accumulated Archard factor ($\sum W$) is written as: [42].

$$\sum W = \sum_{i=1}^N W_{(i)}(Nm) \quad \text{where } W_{(i)} = 4\delta g_{(i)} P_{(i)}(Nm) \quad (1)$$

Where $W_{(i)}$ denotes the dissipated Archard factor at the i th wear cycle.

The corresponding number of wear cycles (i) in Fig. 6 indicate that wear actually began beyond 8 K cycles for both Ni/GPL and steel. After 8 K cycles, the wear rates of the both materials for remaining cycles were observed to be increasing steadily with time but as obvious, during this period the wear rate of steel was quite high compared to Ni/GPL.

Fig. 6 also shows linearly rising trends of wear volumes (V) for Ni/GPL and steel. Wear volume is measured from wear rate (K_V) and accumulated Archard factor ($\sum W$) by using a conventional Archard description as:

$$\Delta V = K_v \times \Delta \left(\sum W \right) \quad (\mu m^3) \quad (2)$$

Table 5 plots the evolution of normalised ‘wear profiles’ and normalised ‘wear depth kinetics profiles’ at various stages of wear degradation for Ni/GPL and steel. The wear profiles showed the ‘U-shaped’ behaviour having a maximum wear depth always at the centre ($x = 0$). It can be seen that at $i = 10,000^{\text{th}}$ cycle, Ni/GPL showed the normalised wear depth = 0.19 while steel showed considerably high normalised wear depth = 0.33. The wear profiles are the moving averages of measured surface interferometric values at various cycles. One such schematic example of interferometric wear profile is shown in red at $i = 10,000$ for Ni/GPL. The 3-D interferometric image for Ni/GPL and steel at $i = 10,000^{\text{th}}$ cycle are shown in Table 5 clearly indicating that Ni/GPL exhibited less severe micro-ploughing wear deformation compared to severe micro-cutting in steel.

Table 5 also displays the computed wear depth kinetics $h_{(i)}(x)$ for Ni/GPL and steel at different wear cycles computed by using corresponding wear profiles. The following incremental equation was used for the development of wear depth kinetics profiles:

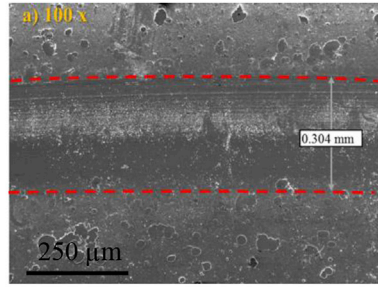
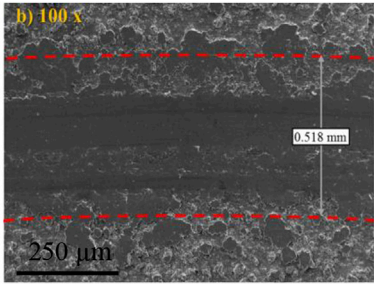
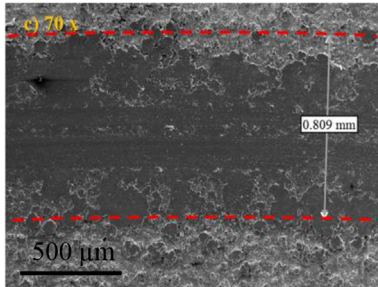
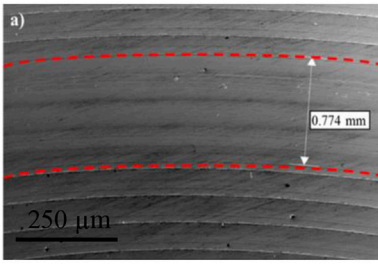
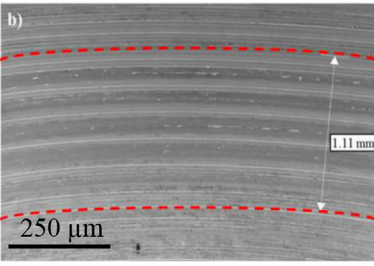
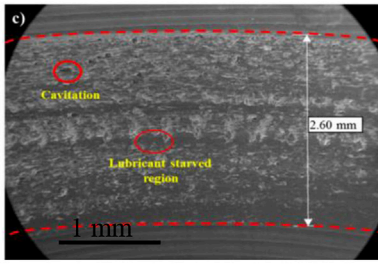
$$h_{(i)}(x) \approx \frac{\Delta h}{\Delta i} = \frac{h_{(i)}(x) - h_{(i-\Delta i)}(x)}{\Delta i} \quad (3)$$

Where Δi is a single wear cycle.

A major decrease of the normalised wear depth kinetics profile corresponding to increasing cycles is observed. For example, at $i = 8000^{\text{th}}$ cycle, the normalised wear depth kinetics for Ni/GPL was 0.21 compared to steel (0.08). One more interesting thing is the evolution behaviour of the normalised wear depth kinetics profile initiating with the elliptical shape decreasing to the hertzian shape and finally becoming a quasi-flat shaped. The contact extremities in quasi-flat distribution ($i = 8000^{\text{th}}$ cycle and onwards) exhibit the type of wear deformation for example micro-ploughing in Ni/GPL showing slightly heightened contact edges while micro-cutting in steel showing almost full flat distribution.

Table 4

The post synergistic-test SEM images of the wear tracks widths for both Ni/GPL and steel 1020 under all the three lubricating oil conditions.

Material	Medium-I	Medium-II	Medium-III
Ni/GPL			
Steel 1020			

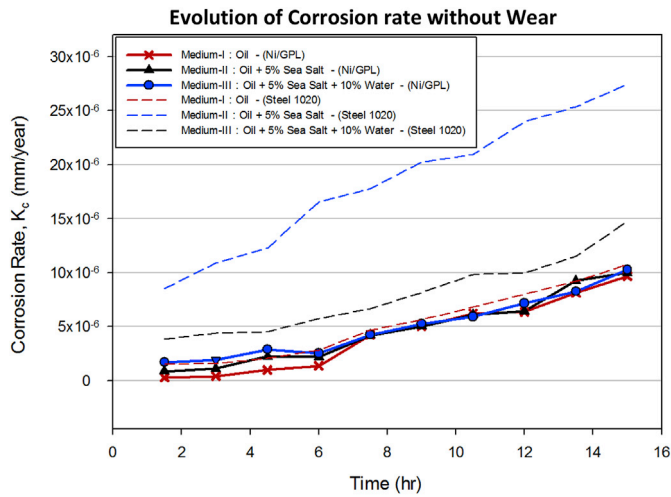


Fig. 5. The evolution of corrosion rates K_C of both Ni/GPL and steel 1020 without wear.

3. A synergistic wear-corrosion model

A step-wise synergistic wear-corrosion model is developed for the nanocomposite coating and can also be used for bulk materials like steel. This model uses the ‘energy profile distribution concept’ of wear depth kinetics presented by Fouvery [43] and integrates it with the nano-mechanics and electrochemical concepts.

As it is evident from the experimental investigations during this research as shown in Table 5, that at the beginning of reciprocating-wear

cycles they display a typical elliptical shape which reduces to hertzian shape, and after a few hundred cycles become a quasi-flat shaped as shown in Fig. 7. The equations of the Archard factor density $W(0)$ ($N\ m/\mu^2$) and accumulated Archard factor density $\sum W(0)$ were developed by correlating the maximum wear depth $h(0)$ (μm) at the wear scar centre (i.e. $x = 0$) in relation to the corresponding wear depth kinetics $h_{(i)}(x)$.

3.1. Archard factor density combined with nano-mechanics

An expression to compute the evolution of accumulated Archard factor density $\sum W(0)$ at the interface centre ($x = 0$) during transition from hertzian/elliptical to flat formulation was developed as shown in eq. (4) [43].

Initially, with no wear at the interface, the Archard factor density $W_{H(i)}$ for hertzian approximation at $x = 0$ assumes that both contact area $a_{(i)}$ and pressure are retained constant with the relative sliding $\delta g_{(i)}$ (Fig. 7 (a)) [44]. Further wear during the i th cycle results in the significant modifications at the interface in addition to contact area extension. Therefore the hertzian distribution of the Archard factor density now transforms in to the elliptical distribution $W_{E(i)}$, but, with the extended contact area $a_{(i)}$ and the relative sliding $\delta g_{(i)}$ (Fig. 7 (b)). Here it is assumed that dissipated Archard factor density at $x = 0$ for both hertzian and elliptical distribution is the same (i.e. $W_{H(i)=E(i)}$) which is formulated according to standard classical solution of contact between a sphere (i.e. the ball) and a half-space (i.e. the scratched coating) [43] as shown in the first part of eq. (4) on the right hand side.

It has been shown in the experimental work presented here, that the Archard parameter distributions become quasi-flat shaped $W_{F(i)}$ after few hundred cycles (Fig. 7 (c)). During the i th cycle the flat contact formulation of dissipated Archard factor density at $x = 0$ is shown in the second part of eq. (4) on the right hand side [43].

$$\sum W(0) = \sum W_{H(i)=E(i)}(0) + W_{F(i)}(0) = \sum_{i=1}^{i_{ft}} \underbrace{\left[\frac{W_{(i)}}{\pi \delta g_{(i)} L} \left(\frac{\delta g_{(i)}}{a_{(i)}} \left(1 - \left(\frac{\delta g_{(i)}}{a_{(i)}} \right)^2 \right)^{\frac{1}{2}} + \arcsin \left(\frac{\delta g_{(i)}}{a_{(i)}} \right) \right) \right]}_{\text{Hertzian /Elliptical approximation}} + \sum_{i=i_{ft}}^N \underbrace{\left[\frac{W_{(i)}}{2a_{(i)} L \left(1 + \frac{\delta g_{(i)}}{2a_{(i)}} \right)} \right]}_{\text{Flat approximation}} \quad (4)$$

Where $W_{(i)}$ and $a_{(i)}$ are the Archard factor dissipated and contact radius of the hertzian, elliptical and flat contacts at the i th cycle. The Archard loading factor density $W_{H(i)=E(i)}(0)$ assumes that the relative sliding $\delta g_{(i)}$ remains lower than the contact radius $a_{(i)}$ (i.e. $\delta g_{(i)} < a_{(i)}$) at a certain normal force applied P.

The contact radius $a_{(i)}$ for the i th wear cycle is given as [43],

$$a_{(i)} = \frac{4PR}{\pi L} \left(\frac{1 - \nu_1^2}{E_1} + \frac{1 - \nu_2^2}{E_2} \right) \times \begin{cases} \text{if } a_{(i)} < a_{ft} \text{ and } i < i_{ft} \text{ then } \sum W(0) = \sum W_{H(i)=E(i)}(0) \\ \text{if } a_{(i)} > a_{ft} \text{ and } i > i_{ft} \text{ then } \sum W(0) = W_{F(i)}(0) \end{cases} \quad (5)$$

Where, a_{ft} and i_{ft} are the critical contact radius and critical cycle respectively, R is the radius of the ball, L is the axial length of the ball/coating contact, ν_1 and ν_2 are the Poisson's coefficient of the coating and the ball respectively, E_1 and E_2 are the Young's modulus of the coating and the ball respectively.

Less than a critical degradation ($a_{(i)} < a_{ft}$) and critical cycle ($i < i_{ft}$), the Archard factor density value is shown by hertzian/elliptical approximation, while higher than a substantial degradation ($a_{(i)} > a_{ft}$) and critical cycle i_{ft} , the flat approximation is taken.

It should be noted that Young's modulus of coating E_1 in eq. (5) is related to the coating surface stress $\sigma_c(0)$ at the centre of wear scar

(interface) and coating surface porosity P_s at the centre of wear scar as [45].

$$P_s = \gamma_s \exp \left(-\frac{\sigma_c(0)}{E_1} \right) \quad (6)$$

$$\sigma_c(0) = E_1 \left(\frac{(E_3 \alpha_s s + E_1 \alpha_c h_c(0)) \Delta T}{(E_3 s + E_1 h_c(0))} + \frac{x - t_b}{\zeta_r} - \alpha_c \Delta T \right) \quad (6a)$$

Where γ_s in eq. (6) is the stress sensitivity coefficient [46].

In Eq. (6) $\sigma_c(0)$ is the biaxial surface stress of the coating at the centre and is given by using Hooke's law given in eq. (6) (a). The residual stress at the coating surface develops when during the wear-cross testing, the coating system with coefficient of thermal mismatch of coating and substrate α_c and α_s respectively is subjected to the temperature change ΔT from its fabrication temperature. Where E_1 , E_3 and α_c , α_s in eq. (6) (a) are the elastic moduli and coefficient of thermal mismatch of coating and substrate respectively; $h_c(0)$ is the thickness of coating at the centre of the wear scar; t_b dictates the location of bending axis and ζ_r is the radius of curvature of coating-substrate system due to residual stress [47].

The average maximum grain size D_{max} of the nanocomposite coating as a function of porosity P_s and volume fraction (f) is [48].

$$D_{max} = D_o + \frac{1}{2} \sqrt{\frac{(1 - P_s)^2 P_s^m \beta}{P_s^3}} \sqrt{\frac{8}{f}} \quad (7)$$

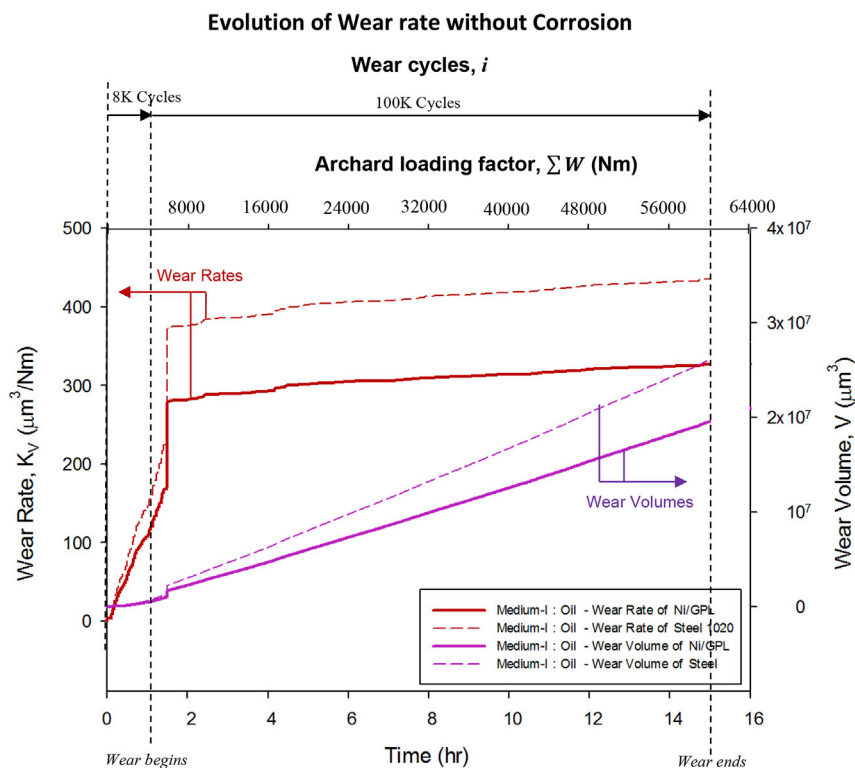


Fig. 6. The evolution of wear rates K_V without corrosion for both Ni/GPL and steel 1020 under uncontaminated oil lubrication condition (Medium-I) only.

Table 5
 The wear depth profiles at different ith wear cycles of Ni/GPL and steel in addition to 3-D interferometric image indicating the type of wear delamination. The Table also shows the computed wear depth kinetics profiles corresponding to wear profiles at different ith wear cycles of Ni/GPL.

Material	Wear depth profiles, Interferometric image and wear depth kinetics profiles
Ni/GPL	<div style="display: flex; justify-content: space-around;"> <div data-bbox="432 314 790 595"> <p>Wear depth profiles</p> </div> <div data-bbox="805 378 1204 585"> <p>3-D Interferometric image -Micro ploughing</p> </div> </div> <div style="text-align: center; margin-top: 20px;"> <p>Wear depth kinetics profiles</p> </div>
Steel 1020	<div style="display: flex; justify-content: space-around;"> <div data-bbox="432 1119 790 1415"> <p>Wear depth profiles</p> </div> <div data-bbox="805 1181 1204 1415"> <p>3-D Interferometric image -Micro-cutting</p> </div> </div> <div style="text-align: center; margin-top: 20px;"> <p>Wear depth kinetics profiles</p> </div>

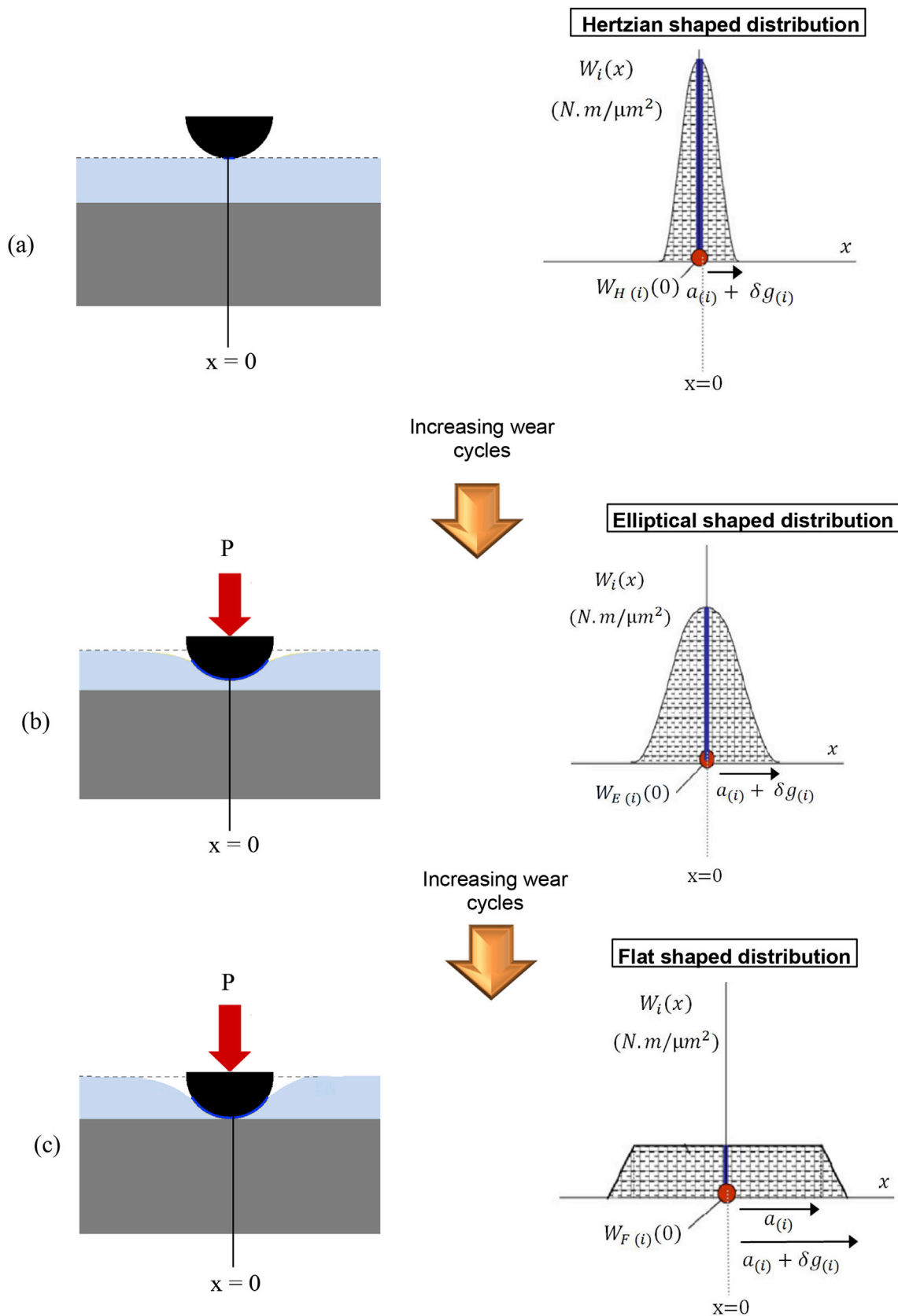


Fig. 7. Sketch of the evolution of analysed Archard factor density $\Sigma W(0)$.

Where β and m represent the material constants. The D_{\max} and D_0 are defined as the sizes of grains after the wear deformation and before the wear deformation respectively. The D_0 is usually the grain size at that particular time when the coating is deposited. The above eq. (7) is derived on an assumption that the particles always remain intact with the grains boundaries even under extreme external pressure which means that D_{\max} is independent of the effect of debris.

3.2. Volume loss owing to wear

The accumulated Archard factor $\sum W$ (eq. (4)) is now utilised to carry out the local investigation of a ball/coating contact. Such analysis involves the formulation of contact radius evolution. Considering the spherical shaped ball, the wear volume V_W (mm^3) is formulated according to geometrical considerations in Fig. 8 as [44]:

$$V_W = \frac{1}{12} \frac{\pi \alpha^4}{R} \left(3 - \frac{h}{R} \right) \quad (8)$$

Where h (mm) is the wear depth. The wear volume V_W (mm^3) is also related to the wear rate K_V (mm^3/Nm) and accumulated Archard factor $\sum W$ (Nm) as:

$$K_V = \frac{V_W}{\sum W} \quad (9)$$

3.3. Volume loss owing to corrosion

The biaxial surface stress $\sigma_c(0)$ (eq. (6) (a)) of the nanocomposite coating at the centre of the wear scar can be written in relation to the current density \vec{J} (A/mm^2) by using a famous Butler-Volmer expression as [49]:

$$\begin{aligned} \vec{J} &= \vec{j}_f - \vec{j}_r = j_o \left[\exp\left(\frac{\alpha Z F \eta}{RT}\right) \exp\left[\frac{2V_m}{3RT} [\sigma_c(0)]\right] - \exp\left(\frac{-(1-\alpha) Z F \eta}{RT}\right) \right] \\ &= j_o \left[\exp\left(\frac{\alpha Z F \eta}{RT}\right) \exp\left(\frac{2V_m}{3RT} \left[E_1 \left(\frac{E_3 \alpha_s s + E_1 \alpha_c h_c(0) \Delta T}{(E_3 s + E_1 h_c(0))} + \frac{x - t_b}{\zeta_r} - \alpha_c \Delta T \right) \right] \right) - \exp\left(\frac{-(1-\alpha) Z F \eta}{RT}\right) \right] \end{aligned} \quad (10)$$

The current density \vec{J} (eq. (10)) is a function of corrosive electrochemical reactions combined with surface stress $\sigma_c(0)$ (eq. (6) (a)).

Where according to the relaxation process of nanocomposite coatings, the intrinsic deformation always occurs in the first five atomic surface layers, whereas most of the atomic layers in the coatings remain undeformed [50] therefore h_s is the thickness of the five atomic surface layers which are directly in contact with the lubricant centre of wear scar (Fig. 9 (a)) and h_c is the thickness of all the atomic layer of nanocomposite coating at the centre of wear scar, j_o is the equilibrium exchange current

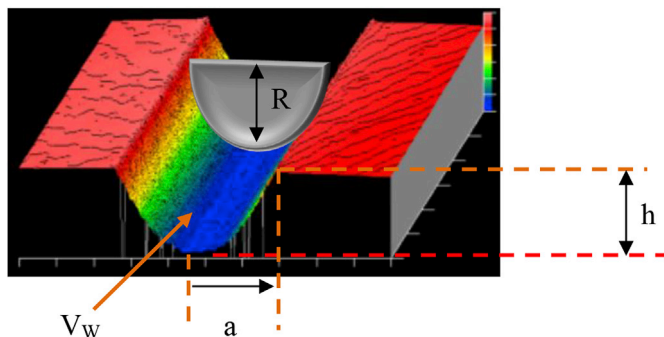


Fig. 8. Schematic of volume loss owing to wear.

density, V_m represent the molar volume, Z is the number of electrons transferred, α indicates the charge transfer coefficient.

The rate of electrochemical reactions on the coating surface can be controlled by the magnitude of surface stress σ_c which can be either compressive or tensile stresses. The volume loss of coating is directly influenced by the current density of the electrochemical reactions.

When the thickness of all the layers of nanocomposite coating approaches as: $h_c \rightarrow \infty$ (Fig. 9 (b)), that is, for the bulk materials (like steel), then eq. (11) can be given as:

$$\vec{J}_{\text{bulk}} = \vec{j}_f - \vec{j}_r = j_o \left[\exp\left(\frac{\alpha Z F \eta + \frac{2\sigma_c(0)V_m}{3}}{RT}\right) - \exp\left(\frac{-(1-\alpha) Z F \eta}{RT}\right) \right] \quad (11)$$

The corrosion current density \vec{J}_{bulk} can be used to calculate volume loss of bulk materials.

The volume loss of nanocomposite coating owing to corrosion V_C (mm^3) can be calculated by using eq. (10) and incorporating it with the Faraday equation. Faraday's law states that volume loss owing to corrosion is a function of corrosion current density \vec{J} as:

$$V_C = \frac{K \vec{J} A_s t}{F \rho} \quad (12)$$

where K is the electrochemical equivalent of specimen material, A_s (mm^2) is the area of the specimen, t (sec) the corrosion time and ρ (g/mm^3) is the density of the nanocomposite coating material.

Eq. (12) can be used to measure the corrosion rate K_C (mm/year) of nanocomposite coating as:

$$K_C = \frac{K \vec{J}}{F \rho} \quad (13)$$

3.4. Synergistic wear-corrosion effect formulation

Synergistic wear-corrosion is “the complex phenomenon combined with mechanical wear and electrochemical factors” and is written as: [51],

$$V = V_W + V_C + S \quad (14)$$

The synergistic wear-corrosion volume loss V is normally written as the summation of mechanical wear volume loss V_W without corrosion (eq. (8)), the corrosion volume loss V_C without wear (eq. (12)) and the synergistic factor S [51].

$$V = V_W + V_C + \Delta V_W + \Delta V_C \quad (15)$$

where ΔV_W is the change in corrosion volume due to wear and ΔV_C is the change in wear volume due to corrosion.

$$V_{W_T} = V_W + \Delta V_W \quad (16)$$

where V_{W_T} is the total wear component of V .

$$V_{C_T} = V_C + \Delta V_C \quad (17)$$

where V_{C_T} is the total corrosion component of V . It should be noted that the effect of corrosive compounds on the sliding wear response has not been considered in this model.

Solving eqs. (8), (12), (14)–(17) gives the corrosion current density of nanocomposite coating as a function of synergistic wear and corrosion parameters as:

$$\vec{J} = \frac{F \rho}{K A_s t} \left(V - \left(K_V \sum W \right) - S \right) \quad (18)$$

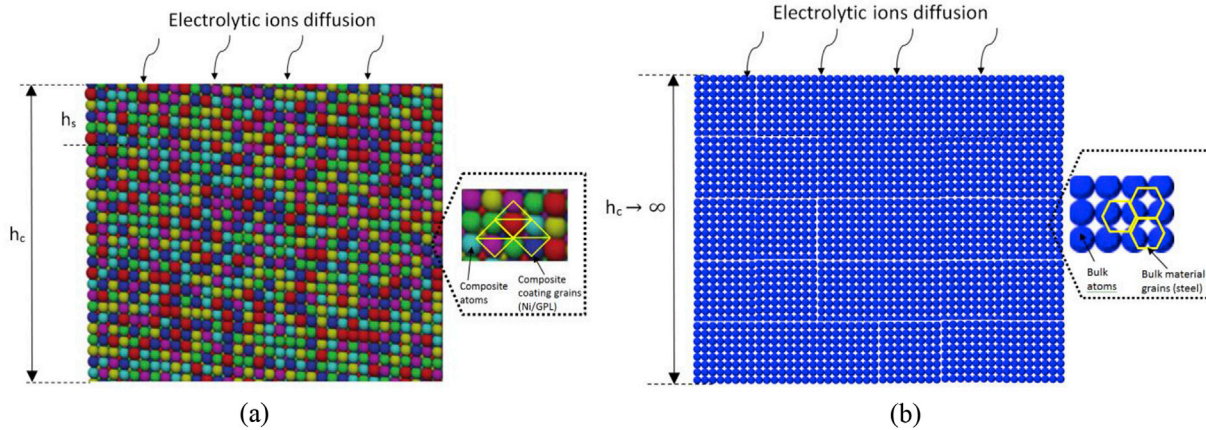


Fig. 9. Schematic representation of atomic layers of (a) nanocomposite coating (for example Ni/GPL) and (b) bulk material (for example steel).

Substituting eq. (18) in eq. (13) gives the synergistic wear-corrosion effect on corrosion rate of nanocomposite coating as:

$$K_{Cw-c} = \frac{V - (K_v \sum W) - S}{A_s t} \quad (19)$$

4. Modelling results and discussion

To validate the reliability and accuracy of the developed model, MD simulations were conducted and compared with the reported experimental results. The second generation of reactive empirical bond order (REBO) potential [19] was used to simulate the Ni/GPL interactions with carbon steel ball via LAMMPS software [52,53]. All crystals were simulated with the embedded-atom method potentials [54,55]. Molecular statics framework was used to conduct all the simulation and conjugate gradient method was used for implementation [55]. The system utilises the NVE microcanonical ensemble boundary conditions [56] which keep the total atoms, volume and energy of system at a constant level.

Fig. 10 is the MD synergistic wear-corrosion simulation model of Ni/GPL and steel 1020. In the simulation, a nanocomposite coating and a counter ball consist of nanocrystalline Ni-matrix and carbon steel respectively. The x-axis is taken parallel to the surface of coating specimen while y-axis is taken normal to the surface as per the right-hand coordinate system. The xy-plane consists of a well-defined atomic arrangement of 1600 atoms set as 80 atoms/layer along the x axis and in a total of 20 layers in depth along y axis. For steel 1020, the above same arrangement of only Fe atoms is used.

A hemispherical carbon steel ball with radius of R = 5 mm is initially

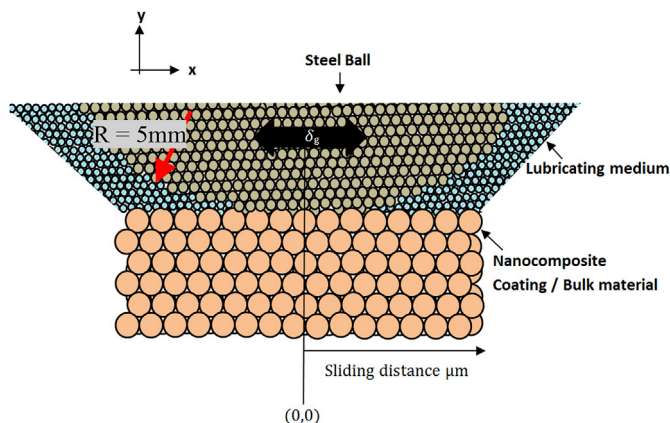


Fig. 10. The MD synergistic wear-corrosion simulation model of Ni/GPL and steel 1020.

indented in the top layer of Ni-matrix at a certain depth. Both carbon steel ball and Ni-matrix are surrounded by lubricating medium, the ionic transport and electrochemical reaction rate of which can be adjusted via Butler-Volmer parameters. After few hundred wear cycles, the ball tip starts wearing out the Ni-matrix with a sliding speed of 0.05 m/sec, same as the experiment. In order to avoid transferring of atoms between Ni-matrix layers and ball tip, the ball is supposed to be relatively rigid.

In this work, wear-corrosion phenomena without plastic deformation are analysed. MD simulations were performed for attaining the material parameter value: ‘m’ for both Ni/GPL and steel 1020. Other material parameters were consulted from respective papers mentioned in Table 6 and were also experimentally verified. All the coating parameters strictly followed the condition that the thickness of coating was 10 μm, as was used in experiment.

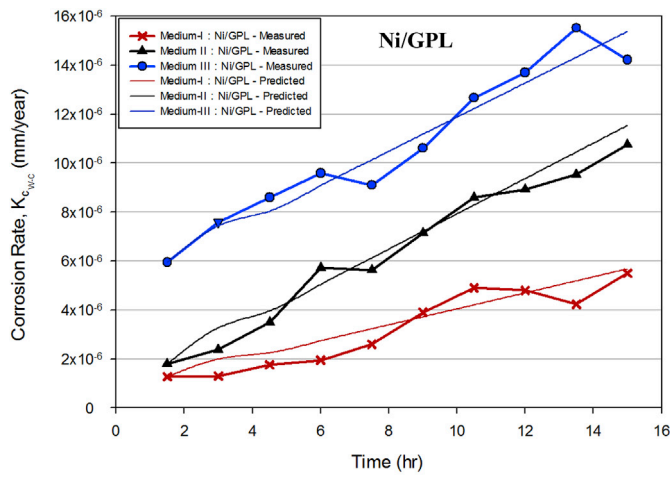
The values in Table 6 are substituted in to developed synergistic wear-corrosion equations to simulate the synergistic wear-corrosion effect on corrosion rates (Fig. 11(a–b)) and current densities (Fig. 12(a–b)) in all three Mediums for both Ni/GPL and steel. The predicted corrosion rates (Fig. 11(a–b)) and current densities (Fig. 12(a–b)) for both Ni/GPL and steel 1020 in all three Mediums were compared with and their respective experimentally measured values for validation. It can be seen that the predicted results and the experimental results show a close relation. Both corrosion rates and current densities were plotted with respect to time. As expected, the predicted corrosion rates for Ni/GPL and steel increased linearly while current densities stabilised after an initial increase as a function of time.

The simulation shows that the model slightly over predicts few data points, which slightly diverges these points away from the experimental values. This divergence however can be minimised by fine-adjustment of material parameter ‘m’ in Table 6.

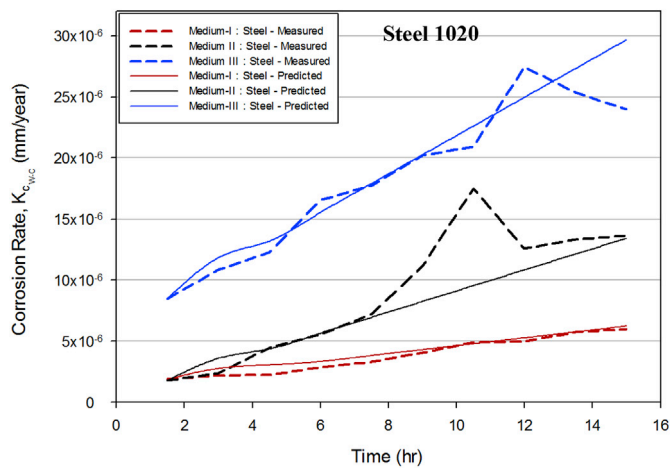
The discussions in this paper will now be focused on the effects of varying ‘nano-mechanics parameters’ such as percentage coating porosity, deposited grain size and thermal mismatch of coating on synergistic wear-corrosion behaviour of Ni/GPL. The predicted current densities for all three Mediums as a function of percentage porosity with respect to time for Ni/GPL are shown in Fig. 13. Fig. 13 clearly shows that

Table 6
Material parameters fitted by using MD simulations.

Materials	ν	E (GPa)	H (HV)	CTE (x 10 ⁻⁶ /K)	m	D ₀ (nm)
Ni/GPL	0.19	240	~480	13.3 [58]	1.5	11.21
	[57]	[38]	[38]			
Steel 1020	0.3	200	126 [39]	11.7 [59]	–	–
	[39]	[39]				
Carbon Steel Ball	0.31	210	520 [60]	6.2 [61]		
	[60]	[60]				

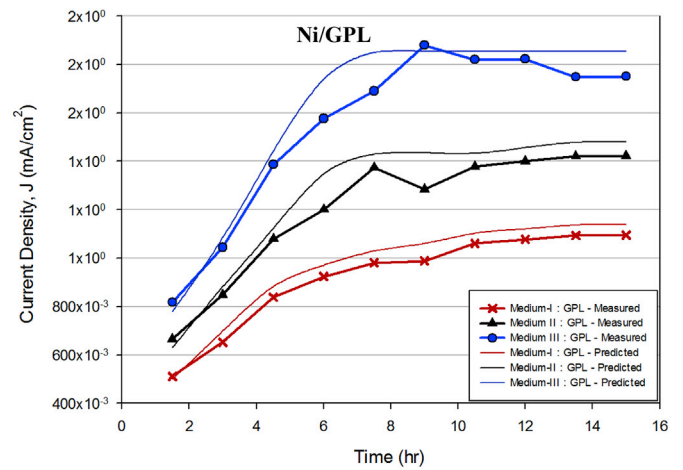


(a)

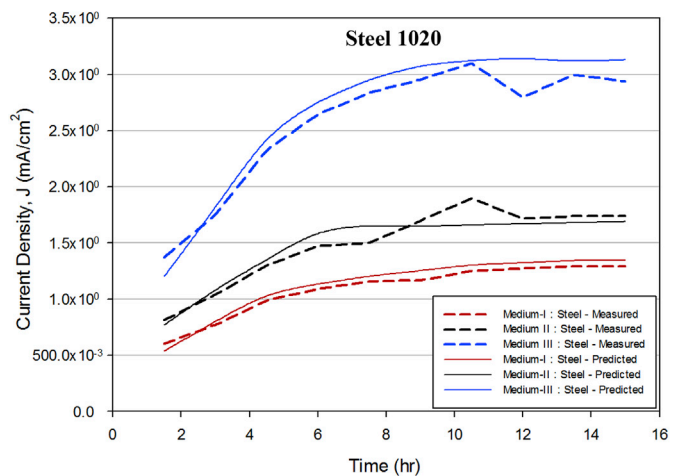


(b)

Fig. 11. The validation of model by comparison of the predicted corrosion rates for both (a) Ni/GPL and (b) steel 1020 in all three Mediums by comparison with their experimentally measured corrosion rates.



(a)



(b)

Fig. 12. The validation of model by comparison of the predicted current densities for both (a) Ni/GPL and (b) steel 1020 in all three Mediums by comparison with their experimentally measured current densities.

the porosity directly influences the overall current densities of Medium-II and III, such that with the increase in percentage porosity from 2 to 6%, a significant rise of 21% and 42% in corrosion rates of Medium-II and III respectively is observed. However for Medium-I the increase in percentage porosity from 2 to 6% results in only 1% rise in corrosion rate. The significant rise in corrosion rates in Medium-II and III with increasing porosity compared to Medium-I is due to large transport of contaminants through pores towards the coating/substrate interface which reduces the adhesion. This reduced adhesion significantly accelerates the corrosion rates of Medium-II and III during synergistic wear-corrosion testing possibly due to weakly adhered debris reaction with contaminants. As Medium-II and III were contaminated therefore porosity increase in Ni/GPL resulted in significant rise in corrosion rates for these two mediums.

Fig. 14 shows the influence of deposited grain size increase on the corrosion rates of Ni/GPL in all the mediums. It can be seen that as the grain size increased by 95% from 11.21 nm to 21.8 nm, significant rise of 24% and 51% in corrosion rates of Medium-II and III respectively is observed. However for Medium-I the increase in grain size results in only 2% rise in corrosion rate. The reason for significant rise in corrosion rates in Medium-II and III for large deposited grain size is that large deposited

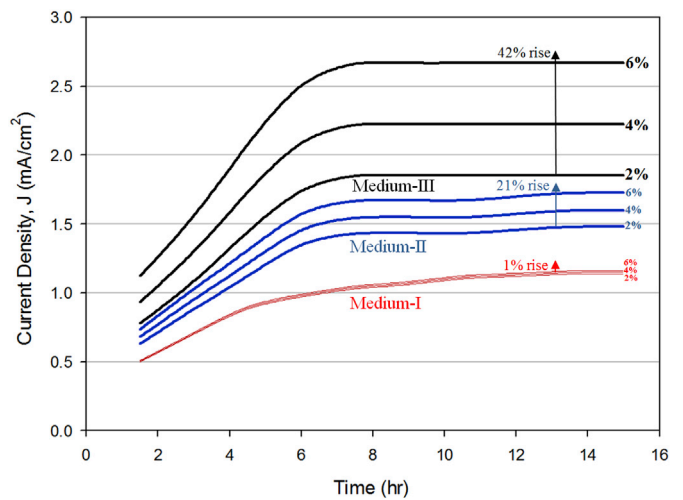


Fig. 13. The predicted current densities for all three Mediums as a function of percentage porosity with respect to time for Ni/GPL.

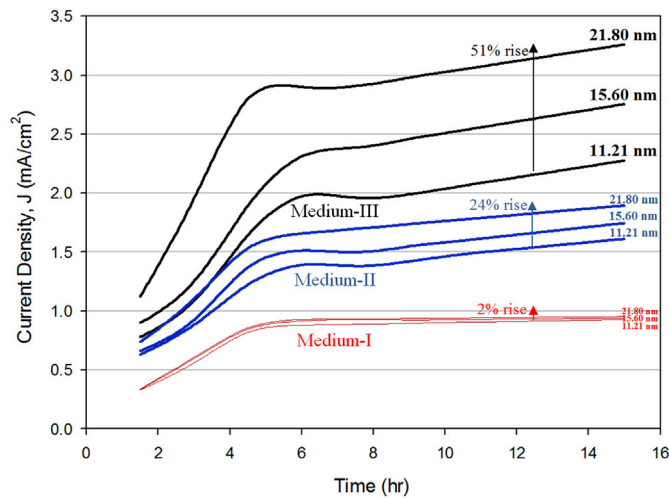


Fig. 14. The predicted current densities for all three Mediums as a function of deposited grain size with respect to time for Ni/GPL.

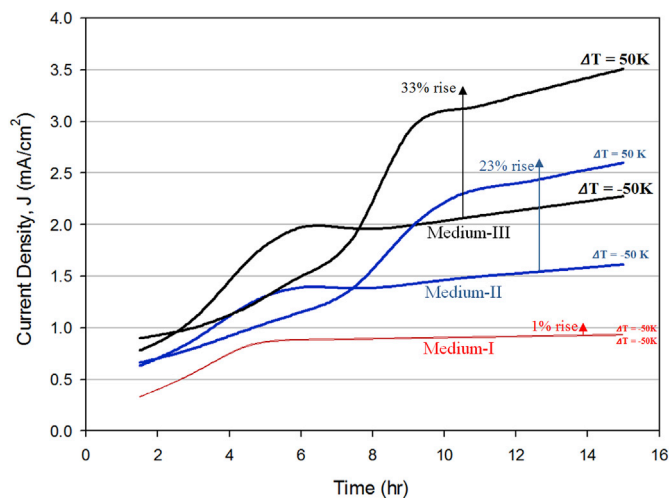


Fig. 15. The predicted current densities for all three Mediums as a function of thermal mismatch with respect to time for Ni/GPL.

grain size exhibits severe cracking which promotes under coat oxidation, and grain pull-out during wear cycles. On the contrary, the small deposited grain size, which are finely dispersed in the Ni-matrix have superior metallurgical bonds preventing coating delamination and hard-particle pull-out. As Medium-I was uncontaminated therefore corrosion rate rise even for large deposited grain size was not significant.

Fig. 15 illustrates the effects of change in temperature ΔT from the coating fabrication temperature on the corrosion rates of Ni/GPL in all the three mediums. The temperature change ΔT induces the residual stress due to the coefficient of thermal elastic (CTE) mismatch between coating and substrate [20]. The wear cycles under such conditions result in higher corrosion rate. Since the thermal mismatch coefficient of Ni/GPL ($\alpha_c = 13.3 \times 10^{-6} \text{ K}^{-1}$) is greater than that of steel substrate ($\alpha_s = 11.7 \times 10^{-6} \text{ K}^{-1}$) [59], the positive temperature diversification ($\Delta T = 50 \text{ K}$) during synergistic testing leads to the development of compressive residual stress in the coating while the negative temperature diversification ($\Delta T = -50 \text{ K}$) leads to the development of tensile residual stress in the coating [20]. The change in ΔT from -50 K to 50 K for Medium II and III results in 23% and 33% rise in corrosion rates respectively. For Medium-I only 1% rise in corrosion rate is observed.

The reason for sigmoid (S-shaped) curves for Medium-II and III at $\Delta T = 50 \text{ K}$ is that under compressive conditions the grain boundaries overlap [62] resulting in low corrosion rate initially before 6 h. However continuous compression under wear cycles beyond 6 h results in surface deformation causing film cracking leading to linear rise in corrosion rate which eventually stabilises after 10 h. Such sigmoid trend is not observed when $\Delta T = -50 \text{ K}$ because continuous tensile stress does not lead to severe cracking thereby avoiding significant rise in corrosion rate with wear cycles [63]. Medium-I did not show sigmoid behaviour at $\Delta T = 50 \text{ K}$ because of the contaminant free medium.

5. Conclusions

This work analyses the synergistic wear-corrosion performance of nanocomposite coating Nickel-Graphene (Ni/GPL) under pure and contaminated lubricating oil conditions, listed in Table 2 and compares it with un-coated steel 1020. Based on this analysis, a novel 2-D predictive model has been developed for predicting the synergetic wear-corrosion reliability of Ni/GPL and steel. The model is equally applicable to any kind of nanocomposite coating and bulk material such as metals.

The following points have been concluded from this study:

- It was observed that for both Ni/GPL and steel the synergistic wear-corrosion effect was negligible in an uncontaminated oil medium. However, for the case of salt plus water contaminated oil medium, the effect of wear-corrosion was significantly evident in steel as compared with Ni/GPL. This is because Ni/GPL has compact and refined grain resulting in minimal transport of corrosive contaminants, water and oxygen which inhibits severe cracking avoiding under coat oxidation, and grain pull-out during wear cycles. Such behaviour of Ni/GPL resulted in small wt% loss compared to steel during synergistic wear-corrosion testing.
- The evolution of ‘corrosion rates without wear’ and ‘wear rates without corrosion’ for both Ni/GPL and steel showed far-better performance of Ni/GPL compared to steel. For the latter, the “U-shaped” wear profiles (Table 5) for maximum wear depth analysis showed relatively high normalised wear depth of steel. This behaviour was also evident by 3-D interferometric micrographs showing severe micro-cutting wear deformation in steel compared to less severe micro-ploughing in Ni/GPL.
- The “U-shaped” wear profiles were used to numerically compute the wear depth kinetics profiles for both Ni/GPL and steel showing the profile evolution beginning with typical elliptical shape reducing to the Hertzian contact and finally converging towards a quasi-flat distribution after 8000 wear cycles. It was found that the steel showed considerably higher decreasing rate profiles compared to Ni/GPL.
- A set of 2-D predictive equations based on the above experimentally computed wear depth kinetics profiles was developed. These equations were integrated with the nano-mechanics and electrochemistry equations to predict the energy distribution (Archard factor density) corresponding to wear depth kinetics profiles based on intrinsic mechanical parameters, such as the porosity, deposited grain size and thermal mismatch of the Ni/GPL.
- The predictions in all the three conditions of lubricating oil were in a good agreement with the experimental results and clearly indicated the elevation in corrosion rate of Ni/GPL with increasing deposited grain size, porosity and thermal mismatch.
- This study provides cutting edge holistic solution for predictive and preventative maintenance techniques applied to complex interacting tribo-systems for wear-corrosion synergism.

Acknowledgments

Authors would like to acknowledge both financial and in-kind support provided by Bournemouth University UK and University of Nevada Reno USA.

References

- [1] Camargo PHC, Satyanarayana KG, Wypych F. Nanocomposites: synthesis, structure, properties and new application opportunities. *Mater Res* 2009;12:1–39.
- [2] Jost P. Economic impact of tribology. In: *Proc mechanical failures prevention group*; 1976. p. 117–39.
- [3] Srivastava M, Grips VW, Rajam K. Influence of SiC, Si₃N₄ and Al₂O₃ particles on the structure and properties of electrodeposited Ni. *Mater Lett* 2008;62:3487–9.
- [4] Thiemig D, Bund A, Talbot JB. Influence of hydrodynamics and pulse plating parameters on the electroco-deposition of nickel–alumina nanocomposite films. *Electrochim Acta* 2009;54:2491–8.
- [5] Low C, Wills R, Walsh F. Electrodeposition of composite coatings containing nanoparticles in a metal deposit. *Surf Coating Technol* 2006;201:371–83.
- [6] Möller A, Hahn H. Synthesis and characterization of nanocrystalline Ni/ZrO₂ composite coatings. *Nanostruct Mater* 1999;12:259–62.
- [7] Karimpoor A, Erb U, Aust K, Palumbo G. High strength nanocrystalline cobalt with high tensile ductility. *Scripta Mater* 2003;49:651–6.
- [8] Gyftou P, Stroumbouli M, Pavlatou E, Asimidis P, Spyrellis N. Tribological study of Ni matrix composite coatings containing nano and micro SiC particles. *Electrochim Acta* 2005;50:4544–50.
- [9] Gül H, Kılıç F, Aslan S, Alp A, Akbulut H. Characteristics of electro-co-deposited Ni–Al₂O₃ nano-particle reinforced metal matrix composite (MMC) coatings. *Wear* 2009;267:976–90.
- [10] Watson S, Friedersdorf F, Madsen B, Cramer S. Methods of measuring wear-corrosion synergism. *Wear* 1995;181:476–84.
- [11] Adler T, Walters R. Corrosion and wear of 304 stainless steel using a scratch test. *Corrosion Sci* 1992;33:1855–76.
- [12] Abd-El-Kader H, El-Raghy S. Wear-corrosion mechanism of stainless steel in chloride media. *Corrosion Sci* 1986;26:647–53.
- [13] Mischler S, Debaud S, Landolt D. Wear-accelerated corrosion of passive metals in tribocorrosion systems. *J Electrochem Soc* 1998;145:750–8.
- [14] Jemmely P, Mischler S, Landolt D. Tribocorrosion behaviour of Fe–17Cr stainless steel in acid and alkaline solutions. *Tribol Int* 1999;32:295–303.
- [15] Jemmely P, Mischler S, Landolt D. Electrochemical modeling of passivation phenomena in tribocorrosion. *Wear* 2000;237:63–76.
- [16] Landolt D, Mischler S, Stemp M. Electrochemical methods in tribocorrosion: a critical appraisal. *Electrochim Acta* 2001;46:3913–29.
- [17] Garcia I, Drees D, Celis J-P. Corrosion-wear of passivating materials in sliding contacts based on a concept of active wear track area. *Wear* 2001;249:452–60.
- [18] Goldberg JR, Gilbert JL. Electrochemical response of CoCrMo to high-speed fracture of its metal oxide using an electrochemical scratch test method. *J Biomed Mater Res* 1997;37:421–31.
- [19] Mischler S, Spiegel A, Landolt D. The role of passive oxide films on the degradation of steel in tribocorrosion systems. *Wear* 1999;225:1078–87.
- [20] Nazir MH, Khan ZA, Saeed A, Stokes K. Modeling the effect of residual and diffusion-induced stresses on corrosion at the interface of coating and substrate. *Corrosion* 2016/04/01;72:500–17. 2015.
- [21] Nazir MH, Khan ZA, Saeed A, Stokes K. A predictive model for life assessment of automotive exhaust mufflers subject to internal corrosion failure due to exhaust gas condensation. *Eng Fail Anal* 2016;63:43–60.
- [22] Nazir MH, Khan ZA, Stokes K. A holistic mathematical modelling and simulation for cathodic delamination mechanism – a novel and an efficient approach. *J Adhes Sci Technol* 2015:1–39.
- [23] Nazir MH, Khan Z, Stokes K. Modelling of metal-coating delamination incorporating variable environmental parameters. *J Adhes Sci Technol* 2014;29:392–423.
- [24] Nazir M, Khan Z, Saeed A, Stokes K. Modelling the effect of residual and diffusion induced stresses on corrosion at the interface of coating and substrate. *Corrosion* 2016;72(4):500–17.
- [25] Nazir MH, Khan ZA, Stokes K. Optimisation of interface roughness and coating thickness to maximise coating-substrate adhesion - a failure prediction and reliability assessment modelling. *J Adhes Sci Technol* 2015;29:1415–45.
- [26] Saeed A, Khan ZA, Nazir MH. Time dependent surface corrosion analysis and modelling of automotive steel under a simplistic model of variations in environmental parameters. *Mater Chem Phys* 2016;178:65–73. 8/1/.
- [27] Nazir M, Khan ZA, Stokes K. A unified mathematical modelling and simulation for cathodic blistering mechanism incorporating diffusion and fracture mechanics concepts. *J Adhes Sci Technol* 2015;29:1200–28.
- [28] Nazir MH, Khan ZA, Stokes K. Analysing the coupled effects of compressive and diffusion induced stresses on the nucleation and propagation of circular coating blisters in the presence of micro-cracks. *Eng Fail Anal* 2016;70:1–15.
- [29] Nazir MH, Saeed A, Khan Z. A comprehensive predictive corrosion model incorporating varying environmental gas pollutants applied to wider steel applications. *Mater Chem Phys* 2017;193:19–34.
- [30] Nazir M, Khan Z. A review of theoretical analysis techniques for cracking and corrosive degradation of film-substrate systems. *Eng Fail Anal* February 2017;72: 80–113.
- [31] Bajwa R, Khan Z, Nazir H, Chacko V, Saeed A. Wear and friction properties of electrodeposited Ni-Based coatings subject to nano-enhanced lubricant and composite coating. *Acta Metall Sin* 2016;29:902–10.
- [32] Nazir MH, Khan Z. Maximising the interfacial toughness of thin coatings and substrate through optimisation of defined parameters. *Int. J. Comput. Meth. Exp. Meas.* 2015;3:316–28.
- [33] Bajwa RS, Khan Z, Bakolas V, Braun W. Effect of bath ionic strength on adhesion and tribological properties of pure nickel and Ni-based nanocomposite coatings. *J Adhes Sci Technol* 2016;30:653–65.
- [34] Bajwa RS, Khan Z, Bakolas V, Braun W. Water-Lubricated Ni-Based composite (Ni–Al₂O₃, Ni–SiC and Ni–ZrO₂) thin film coatings for industrial applications. *Acta Metall Sin* 2015;29:8–16.
- [35] Nazir MH, Khan ZA, Saeed A, Bakolas V, Braun W, Bajwa R, Rafique S. Analyzing and modelling the corrosion behavior of Ni/Al₂O₃, Ni/SiC, Ni/ZrO₂ and Ni/Graphene nanocomposite coatings. *Materials* 2017;10:1225.
- [36] Prince M, Thanu AJ, Gopalakrishnan P. Improvement in wear and corrosion resistance of AISI 1020 steel by high velocity oxy-fuel spray coating containing Ni-Cr-B-Si-Fe-C. In: *High temperature materials and processes*, vol. 31; 2012. p. 149.
- [37] Jabbar A, Yasin G, Khan WQ, Anwar MY, Korai RM, Nizam MN, Muhyodin G. Electrochemical deposition of nickel graphene composite coatings: effect of deposition temperature on its surface morphology and corrosion resistance. *RSC Adv* 2017;7:31100–9.
- [38] Ren Z, Meng N, Shehzad K, Xu Y, Qu S, Yu B, Luo J. Mechanical properties of nickel-graphene composites synthesized by electrochemical deposition. *Nanotechnology* 2015;26:065706.
- [39] Harvey PD. *Engineering properties of steel*: Asm Intl. 1982.
- [40] Selcuk B, Ipek R, Karamış M. A study on friction and wear behaviour of carburized, carbonitrided and borided AISI 1020 and 5115 steels. *J Mater Process Technol* 2003;141:189–96.
- [41] Aneja KS, Böhm HM, Khanna A, Böhm S. "Functionalised graphene as a barrier against corrosion. *FlatChem* 2017;1:11–9.
- [42] Kalin M, Vizić J, Novak S, Dražić G. Wear mechanisms in oil-lubricated and dry fretting of silicon nitride against bearing steel contacts. *Wear* 1997;210:27–38.
- [43] Fourny S, Liskiewicz T, Paulin C. A global-local wear approach to quantify the contact endurance under reciprocating-fretting sliding conditions. *Wear* 2007;263: 518–31.
- [44] Schwarz UD. A generalized analytical model for the elastic deformation of an adhesive contact between a sphere and a flat surface. *J Colloid Interface Sci* 2003; 261:99–106.
- [45] Witherspoon PA, Wang JS, Iwai K, Gale JE. Validity of cubic law for fluid flow in a deformable rock fracture. *Water Resour Res* 1980;16:1016–24.
- [46] Lei Q, Xiong W, Yuang J, Cui Y, Wu Y-S. Analysis of stress sensitivity and its influence on oil production from tight reservoirs. In: *Eastern regional meeting*; 2007.
- [47] Xuan F-Z, Cao L-Q, Wang Z, Tu S-T. Mass transport in laser surface nitriding involving the effect of high temperature gradient: simulation and experiment. *Comput Mater Sci* 2010;49:104–11.
- [48] Seok H-K, Park K-W, Lee J-C. Particle size versus grain size relation in the sprayformed Al-18Si composites. *Met Mater Int* 2009;15:609–13.
- [49] Gutman EM. *Mechanochemistry of materials*. Cambridge Int Science Publishing; 1998.
- [50] Zhang T-Y, Ren H, Wang Z-J, Sun S. Surface eigen-displacement and surface Poisson's ratios of solids. *Acta Mater* 2011;59:4437–47.
- [51] Iwabuchi A, Lee JW, Uchidate M. Synergistic effect of fretting wear and sliding wear of Co-alloy and Ti-alloy in Hanks' solution. *Wear* 2007/09/10;263:492–500.
- [52] "http://lammps.sandia.gov".
- [53] Plimpton S. Fast parallel algorithms for short-range molecular dynamics. *J Comput Phys* 1995;117:1–19.
- [54] Foiles S, Baskes M, Daw M. Embedded-atom-method functions for the fcc metals Cu, Ag, Au, Ni, Pd, Pt, and their alloys. *Phys Rev B* 1986;33:7983.
- [55] Mendeleev M, Han S, Srolovitz D, Ackland G, Sun D, Asta M. Development of new interatomic potentials appropriate for crystalline and liquid iron. *Phil Mag* 2003;83: 3977–94.
- [56] Goel S, Faisal NH, Ratia V, Agrawal A, Stukowski A. Atomistic investigation on the structure–property relationship during thermal spray nanoparticle impact. *Comput Mater Sci* 2014;84:163–74.
- [57] Politano A, Chiarello G. Probing the Young's modulus and Poisson's ratio in graphene/metal interfaces and graphite: a comparative study. *Nano Research* 2015; 8:1847–56.
- [58] Sigmund O, Torquato S. Composites with extremal thermal expansion coefficients. *Appl Phys Lett* 1996;69:3203–5.
- [59] Lide DR. *CRC handbook of chemistry and physics*. 12J204. 1947.
- [60] "Automation Creations, Inc.. (2017). *MatWeb, Your Source for Materials Information*, <http://www.matweb.com/>. Retrieved at November 23, 2017, from the website temoa : Open Educational Resources (OER) Portal at http://www.matweb.com/search/datasheet_print.aspx?matguid=ee25302df4b34404b21ad67f8a83e858."
- [61] Novikova SI. Thermal expansion of solids. Moscow Izdatel Nauka; 1974.
- [62] TobyáKelsey E, áde Leeuw NH. Atomistic simulation of dislocations, surfaces and interfaces in MgO. *J Chem Soc, Faraday Trans* 1996;92:433–8.
- [63] Read WT, Shockley W. Dislocation models of crystal grain boundaries. *Phys Rev* 1950;78:275.